coatings

MDPI

Article

Cost-Effective Nanoporous Gold Obtained by Dealloying Metastable Precursor, Au33Fe67, Reveals Excellent Methanol Electro-Oxidation Performance

Deepti Raj, Federico Scaglione *, Gianluca Fiore and Paola Rizzi

Dipartimento di Chimica e Centro Interdipartimentale NIS (Nanostructured Surfaces and Interfaces), Università di Torino, Via Pietro Giuria 7, 10125 Torino, Italy; deepti.raj@unito.it (D.R.); gianluca.fiore@unito.it (G.F.); paola.rizzi@unito.it (P.R.)

* Correspondence: federico.scaglione@unito.it

Abstract: In this study, we report nanoporous gold (NPG) as an economic, efficient, and stable alternative electrocatalyst for methanol electro-oxidation. The said sample was successfully prepared from an Fe-rich metastable $Au_{33}Fe_{67}$ supersaturated solid solution acting as the precursor, which was formed into ribbons by the phenomenon of rapid solidification using melt-spinning technique. The as-quenched ribbon was then chemically dealloyed in 1 M HCl at 70 °C for different durations of time. A homogeneous, free-standing, and mechanically stable NPG sample was obtained with tunable ligament shape and size. The morphology and composition were characterized by using SEM with EDS, while the structure by XRD. The sample was examined as an electrocatalyst for methanol electro-oxidation profiting off its large surface area; cyclic voltammetry (CV) was the technique employed for electrochemical studies. In a basic solution of methanol and KOH, the sample displays a low peak potential of 0.47 V vs. Ag/AgCl for methanol electro-oxidation with a high peak current density of 0.43 mA/cm^2. In addition, it demonstrates outstanding stability and high poisoning tolerance. It is noteworthy that the fabrication process of the NPG sample from start to end was intentionally opted to be sustainable, cost-effective, rapid, and feasible. The usage of critical raw materials was avoided. As a whole, the properties and results put forth by the NPG sample make it an inexpensive, sustainable, and excellent alternative as an electrocatalyst for methanol electro-oxidation.

Keywords: nanoporous gold; Au–Fe; dealloying; ethanol electro-oxidation; electrocatalyst

Citation: Raj, D.; Scaglione, F.; Fiore, G.; Rizzi, P. Cost-Effective Nanoporous Gold Obtained by Dealloying Metastable Precursor, Au33Fe67, Reveals Excellent Methanol Electro-Oxidation Performance. *Coatings* **2022**, *12*, 831. https://doi.org/10.3390/coatings12060831

Academic Editor: Jinyang Xu

Received: 28 April 2022
Accepted: 10 June 2022
Published: 14 June 2022

1. Introduction

Nanoporous (NP) metals have been well renowned as a tremendously favorable class of materials employed extensively in a wide array of fields, such as fuel cells, sensors, catalysis, hydrogen storage, and molecular sieves [1–3]. Credit goes to their unique physical and chemical properties, such as high surface area-to-volume ratio, high thermal conductivity, high electrical conductivity, corrosion resistance, and fatigue resistance [4,5]. Their morphology is built of a 3D framework of nanosized ligaments and pores [1]. Among all NP metals, nanoporous gold (NPG) is extremely promising. Its high and tunable porosity, high specific surface area, good structural stability, high number of active sites, high conductivity, facile preparation, and biocompatibility are some of its highlighting properties, which make it quite a worthy candidate in a number of applications, such as catalysis, sensing, and materials for energy conversion to bio-related applications [6,7].

Dealloying has gathered enough popularity as a straightforward technique for fabricating NP metals. It is a controlled etching where the less noble metal is selectively removed from the alloy while the atoms of the remnant more noble metal self-assemble into interconnected ligaments and open pores with random spatial arrangement by surface diffusion [5,8]. The morphology of the obtained NP metal depends on the type of alloy—crystalline or amorphous [9,10]. Dealloying a crystalline alloy results in a porous

single crystal evolved from each grain, while for an amorphous alloy, ligaments are formed from the impingement of several fine crystals [9,11–13]. The most commonly performed dealloying techniques are chemical and electrochemical dealloying. One of the important parameters to consider for successful dealloying is the parting limit defined as the minimum concentration of the more noble component in the alloy above which parting cannot occur [1,14,15]. By varying the experimental conditions (i.e., duration of dealloying, type and pH of electrolyte, and temperature of the process), one can feasibly obtain NP metals of specific pore and ligament size and shape [16–18].

The main reasons for the choice of Fe to be alloyed with Au were its (i) abundant and cheap availability, (ii) mechanical strength, and (iii) easy selective dissolution using common electrolytes in simple experimental conditions. The master alloy was consciously and carefully prepared of an Fe-rich composition with the target of diminishing the amount of expensive Au as much as possible, abiding by the parting limit. In accordance with the Au–Fe equilibrium phase diagram, the composition was set at 33 at. % Au and 67 at. % Fe. Since Fe and Au have an extended miscibility gap in the solid state according to the phase diagram, precursor alloy was forced to form a metastable supersaturated solid solution using the rapid solidification technique [19].

The incessant global energy needs have compelled the development of renewable, sustainable, and efficient alternatives to fossil fuel resources [20–23]. In this regard, direct methanol fuel cells (DMFCs) have garnered exploding intrigue over the past years towards the production of sustainable energy [24,25]. DMFCs are electrochemical devices that convert the chemical energy of methanol in electric energy via methanol electro-oxidation [11]. Methanol being a liquid under ambient conditions, in addition to its high specific energy, easy storage, low toxicity, lower cost, near room working temperature, and abundant production, makes for a brilliant energy source [25–27]. The methanol electro-oxidation reaction can be categorized into acidic and alkaline depending on the pH of the supporting electrolyte [24]. The methanol electro-oxidation reaction is the most integral part of DMFCs that takes place at the anode side of a DMFC [25]. The conventional electrocatalysts include Pt-based ones, such as Pt–Cu and Pt–Ru alloys [25,28]. However, Pt certainly has its disadvantages, for instance, expensiveness, instability, and susceptibility to poisoning [26,29–31]. Developing a sustainable electrocatalyst with low cost, enhanced activity, and high durability, thus, becomes crucial [26]. Efforts have been made to find performing electrode alternatives to Pt and Pt-based alloys [32–35]. In this thread, NPG stands out as the cheaper alternative supported by its nobility, resistance to surface oxidation, and large surface area-to-volume ratio [25].

In this paper, a metastable supersaturated solid solution of $Au_{33}Fe_{67}$ was taken as a cheap precursor for the fabrication of NPG by chemically dealloying in 1 M HCl at 70 °C for different durations of time. Methanol electro-oxidation was reported using one of the NPG samples on the strength of its large surface area-to-volume ratio and typically high number of active sites. The results make a good case for the employability of NPG samples in the application of methanol electro-oxidation.

2. Materials and Methods

Arc-melting technique was employed to prepare the $Au_{33}Fe_{67}$ master alloys of nominal composition 33 at. % Au and 67 at. % Fe using metals (99.99% Au and 99.95% Fe) after evacuating and purging the furnace several times in Ti-gettered Ar atmosphere. Then, the obtained ingot was rapidly solidified by melt-spinning technique to form ribbons. The molten ingot was ejected through the nozzle of a quartz crucible of 2 mm size onto the hardened Cu wheel (distance to wheel being 1.5 mm) of the melt-spinning apparatus at a linear speed of 25 m s^{-1} in a closed chamber under Ar atmosphere (chamber pressure was 1 bar, while overpressure was + 0.2 bar). The ribbon was completely ejected in a few seconds, which was long, continuous, and homogeneous with a thickness of approximately 15 µm and a width of 8 mm.

The as-quenched ribbon was chemically dealloyed in 1 M HCl at 70 °C for durations of 8 to 16 h. These samples were named, respectively, NPG_8h, NPG_12h, NPG_14h, and NPG_16h. All samples were washed in deionized water several times and dried in air. All electrolytes were prepared from chemical-grade reagents and deionized water.

Structural and compositional investigations of the master alloy, as-quenched ribbon, and as-dealloyed samples, before and after treatments, were performed using a PANalytical X'pert X-ray Diffractometer in Bragg–Brentano geometry with monochromatic Cu Kα radiation, scanning electron microscopy (Inspect SEM, FEI), field-emission scanning electron microscopy (FIB-FE-SEM/EBSD/EDS/TOF-SIMS Tescan S9000G microscope), and energy dispersive X-ray spectroscopy (Oxford Ultim-Max 100 connected to FE-SEM).

Studies of the metallography of the nanoporous samples were conducted using the open source ImageJ, a software for processing and analyzing scientific images; in particular, the average ligament size was measured at the narrower neck of the ligaments by analyzing 200 ligaments per sample [13,36].

To examine the electrocatalytic activity of the as-dealloyed samples at room temperature, a solution of 0.5 M KOH and 5 M CH_3OH was taken as the electrolyte. The cell setup consisted of the standard three-electrode cell configuration (i.e., saturated Ag/AgCl double-bridge reference electrode, Pt-grid counter-electrode, and the as-dealloyed sample as the working electrode). The cell was connected to a potentiostat, PGSTAT302N Autolab Metrohm. Preceding the electrocatalytic measurement, the concerned sample was immersed in concentrated HNO_3 (65%) for 15 min, then rinsed in deionized water for 15 min to remove the acid inside pores completely. This process activates the sample preparing it for the electrocatalytic experiment [15]. Next, the sample underwent 500 cycles of potentiodynamic scans at a sweeping rate of 20 mV/s from −0.1 to 0.7 V vs. Ag/AgCl. To have an estimation of the electrochemically active surface area (EASA) of the NPG samples, electrochemical oxidation of 0.5 M KOH using cyclic voltammetry (CV) was performed at a scan rate of 20 mV s^{-1} from −0.13 to 0.5 V vs. Ag/AgCl [37–39]. The reduction peak of the CV curve was integrated to calculate the area under the graph. This area reveals the amount of electrochemically active sites, hence giving the EASA [40]. This EASA was later used to normalize the obtained current density. All the potentials were reported with respect to the Ag/AgCl electrode.

3. Results and Discussion

3.1. As-Quenched Ribbon Characterization

A piece of an as-quenched ribbon in a cross section was embedded in resin and mirror-polished, and its microstructure was observed in SEM backscattered electron images (SEM-BSE). The cross section in Figure 1a shows two visibly different areas: a finer microstructure can be seen on the wheel-side area, while a coarser one appears to constitute the air side with a distinguishable line of change of the microstructure in the middle of the ribbon. This can be credited to the fact that higher quenching rates act in contact with the wheel during solidification with respect to the air side where the heat extraction from the liquid is comparatively slower and not as effective [41].

As displayed in Figure 1b, the wheel side is constituted by a matrix with embedded precipitates, while in Figure 1c, the air side is showcasing dark dendritic grains surrounded by a white matrix with embedded precipitates. This microstructure on the air side is composed of two phases, as seen in Figure 1c: bcc α(Fe) (dark dendritic regions named 1) and fcc (Au) (brighter matrix, named 3). As the miscibility gap is reached during cooling, lamella-like microstructures with alternated grains of bcc α(Fe) and fcc (Au) are visible in the darker dendritic regions (number 2 in Figure 1c). Precipitates of bcc α(Fe) are also observed in fcc (Au) as darker acicular structures in bright regions. The targeted composition of the as-quenched ribbon was achieved as confirmed by EDS analysis (i.e., 33 at. % Au and 67 at. % Fe).

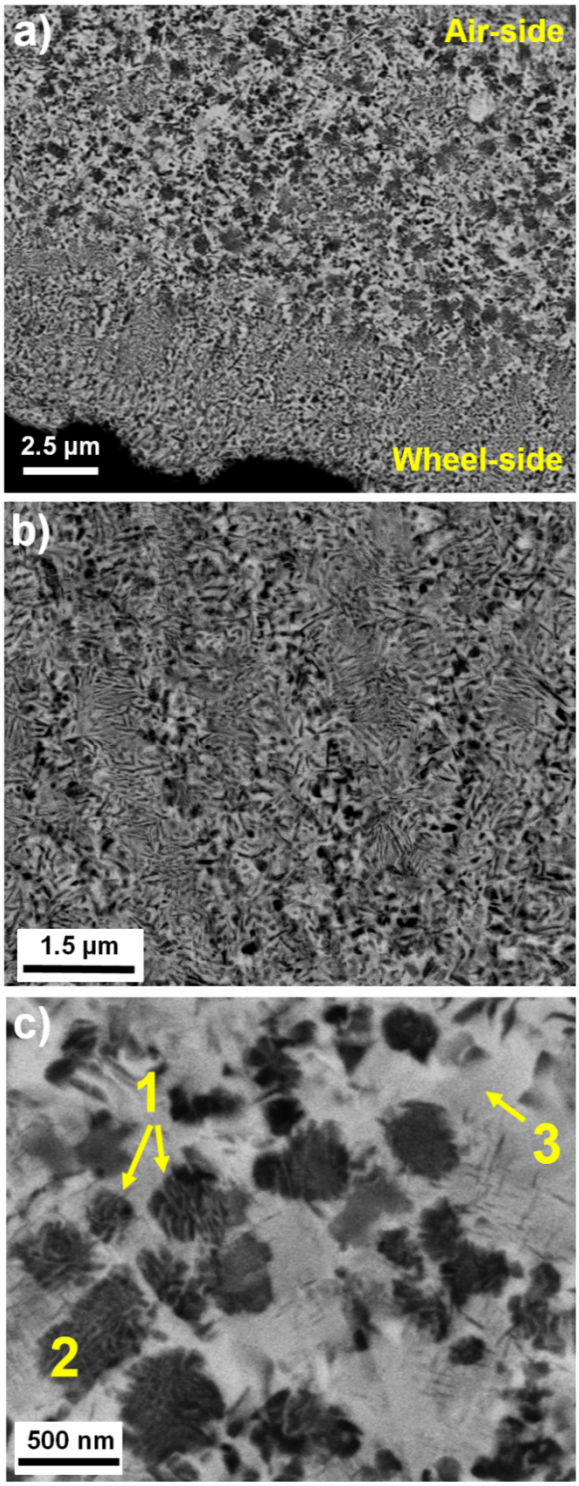

Figure 1. SEM-BSE image of the as-quenched $Au_{33}Fe_{67}$ ribbon (**a**) cross section, (**b**) wheel side of the cross section, and (**c**) air side of the cross section; number 1 denotes bcc α(Fe) phase, number 2 denotes alternated grains of bcc α(Fe) and fcc (Au) phases; and number 3 denotes fcc (Au) phase.

Figure 2a shows the XRD pattern of the as-quenched ribbon, where the phases in the microstructure of the ribbons described earlier are established. It quite evidently shows the peaks corresponding to the metastable supersaturated solid solutions fcc (Au) and bcc α(Fe). It is known that the lattice parameter of fcc (Au) decreases as Fe atoms are incorporated in the Au matrix. This leads to a shift in the peak positions towards higher diffraction angles with respect to the pure Au [42]. Similarly, the lattice parameter of the

bcc α(Fe) solid solution undergoes an enhancement, with respect to pure Fe, so that Fe the lattice can accommodate Au atoms, which results in peaks shifted towards smaller diffraction angles. The lattice parameters of Au and Fe in the as-quenched ribbon calculated as 3.986 and 2.942 nm, respectively, also substantiate the shift in the peaks.

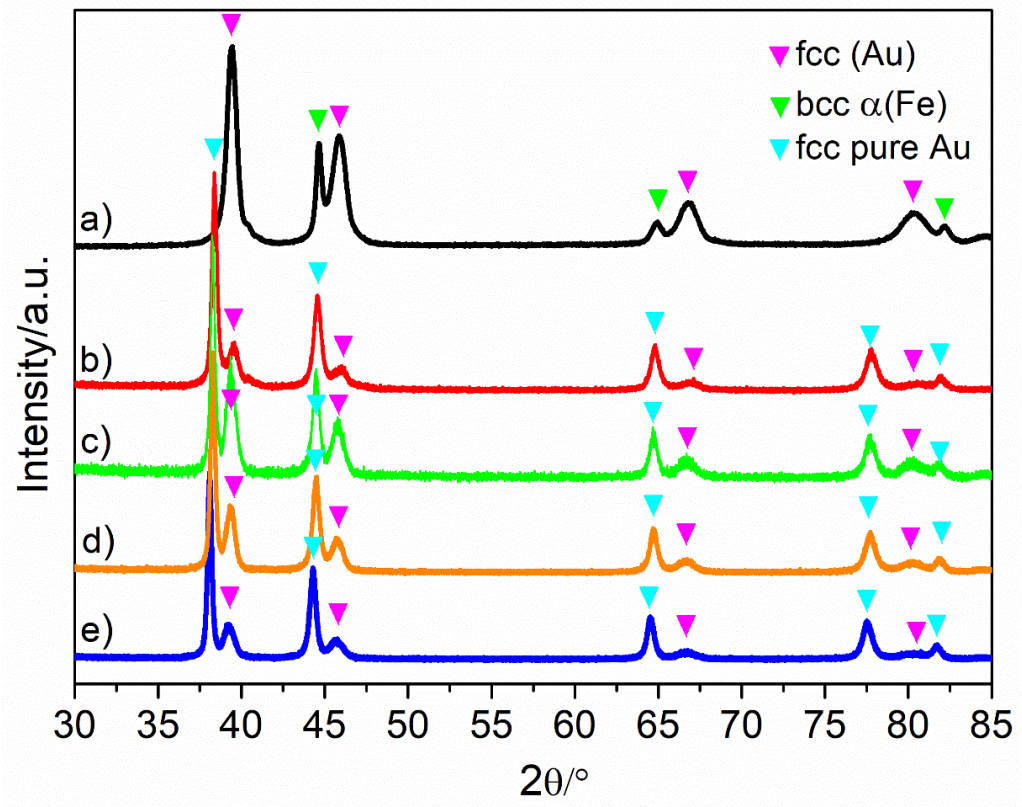

Figure 2. XRD patterns of (**a**) the as-quenched ribbon, (**b**) NPG_8h, (**c**) NPG_12h, (**d**) NPG_14h, and (**e**) NPG_16h.

3.2. Chemical Dealloying and Nanoporous Gold

Ribbons of a couple of centimeters were taken from the as-quenched ribbon and chemically dealloyed in 1 M HCl at 70 °C for 8, 12, 14, and 16 h. The structure of the NPG was studied by diffraction. The XRD pattern of all samples is reported in Figure 2. The patterns (b) to (e) show reflections of a new fcc pure Au phase that is generated by the surface diffusion of gold ad-atoms during the dealloying process; the lattice parameter is approaching that of pure Au signaling towards the formation of Au-rich ligaments. The creation of the ligamentous framework takes place, simultaneously with the bcc α phase removal by galvanic effect, being the less noble phase in the alloy, and reflections disappear from the pattern after dealloying. Interestingly, the pristine fcc (Au) phase decreases in intensity during the etching, but it is still present as deduced by the lower-intensity yet visible peaks, which are slightly shifted to low angles due to the removal of iron content and consequent increasing of the lattice parameter. However, comparing the intensities of peaks related to this pristine fcc (Au) in samples prepared at different dealloying times, it is not possible to find a clear decreasing trend; this is due to the different dimension of the NPG used for the XRD measurements, thus effecting the number of counts. This reveals that a certain amount of the non-dealloyed fcc (Au) phase remains unaffected under the Au ligaments formed during dealloying.

The evolution of ligament morphology as a function of the dealloying time was investigated by SEM in secondary electron mode (SEM-SE), and images for all the as-dealloyed samples are presented in Figure 3.

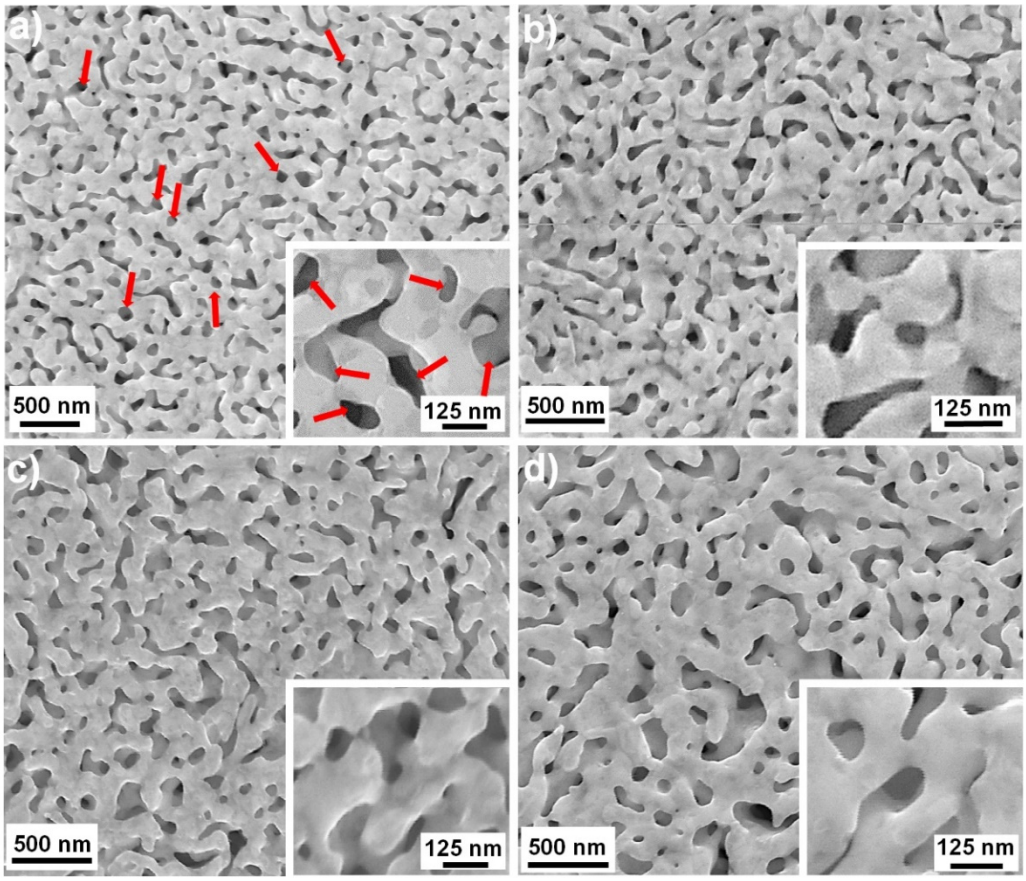

Figure 3. SEM-SE images of the surface view of (**a**) NPG_8h, (**b**) NPG_12h, (**c**) NPG_14h, and (**d**) NPG_16h.

It is discernible in Figure 3a that the sample NPG_8h very evidently adopted a widespread bicontinuous homogeneous nanoporous morphology consisting of an interconnected framework of ligaments and many small pores. The red arrows point towards some of the pores present in the morphology. It should be noted that this kind of morphology is quite typical of NPG samples as previously reported in the literature. For NPG_12h (Figure 3b), a bimodal morphology seems to be prevalent, composed of majority of thick ligaments with small portions of thinner ligaments. There is also some coarsening seen on the surface. A variation in the distribution of Au and Fe content in the as-quenched ribbon could be a reason behind this, which affects the kinetics of dealloying, resulting in thicker or thinner ligaments. As the duration of the dealloying treatment is increased, the surface morphology homogenizes in the case of NPG_14h. On increasing the dealloying time further, this effect is augmented. The ligaments diffuse into neighboring regions, coalesce, and form thicker and bigger ligaments, resulting in an overall coarsened nanoporous morphology, visible in the case of NPG_16h. Overall, these images in Figure 3 serve as proof of the porosity present in the samples.

Cross-sectional SEM images of NPG_8h, NPG_12h, NPG_14h, and NPG_16h are also provided in Figure S1 of the Supplementary Materials, where small pores and ligaments are widespread. It can be inferred that dealloying was achieved only partially in the cross section for NPG_8h shown by the nanoplates/nanosheets observed in the SEM image. A possible reason could be that the dealloying time is not enough to facilitate complete dealloying. Therefore, when the dealloying time is increased, the samples become more Au-rich in composition and ultimately, and NPG_16h reaches the maximum degree of dealloying, giving 91 at. % of Au as determined by EDS. The EDS analysis in terms of the Au composition gives the value 75 at. % for NPG_8h, 85 at. % for NPG_12h, 88 at. % for NPG_14h, and 91 at. % for NPG_16h, also reported in Figure 4f. It is well known

in the field of dealloying that a complete removal of the non-noble counterpart is hardly achieved when the precursor is a crystalline material. Statistical analysis of ligaments with histograms and distributions is reported for all samples in Figure 4a–d. A general increasing trend was observed as a function of dealloying time; indeed, the distribution curves are shifted to higher values of ligament dimension. The average ligament size is reported in Figure 4e within the standard error.

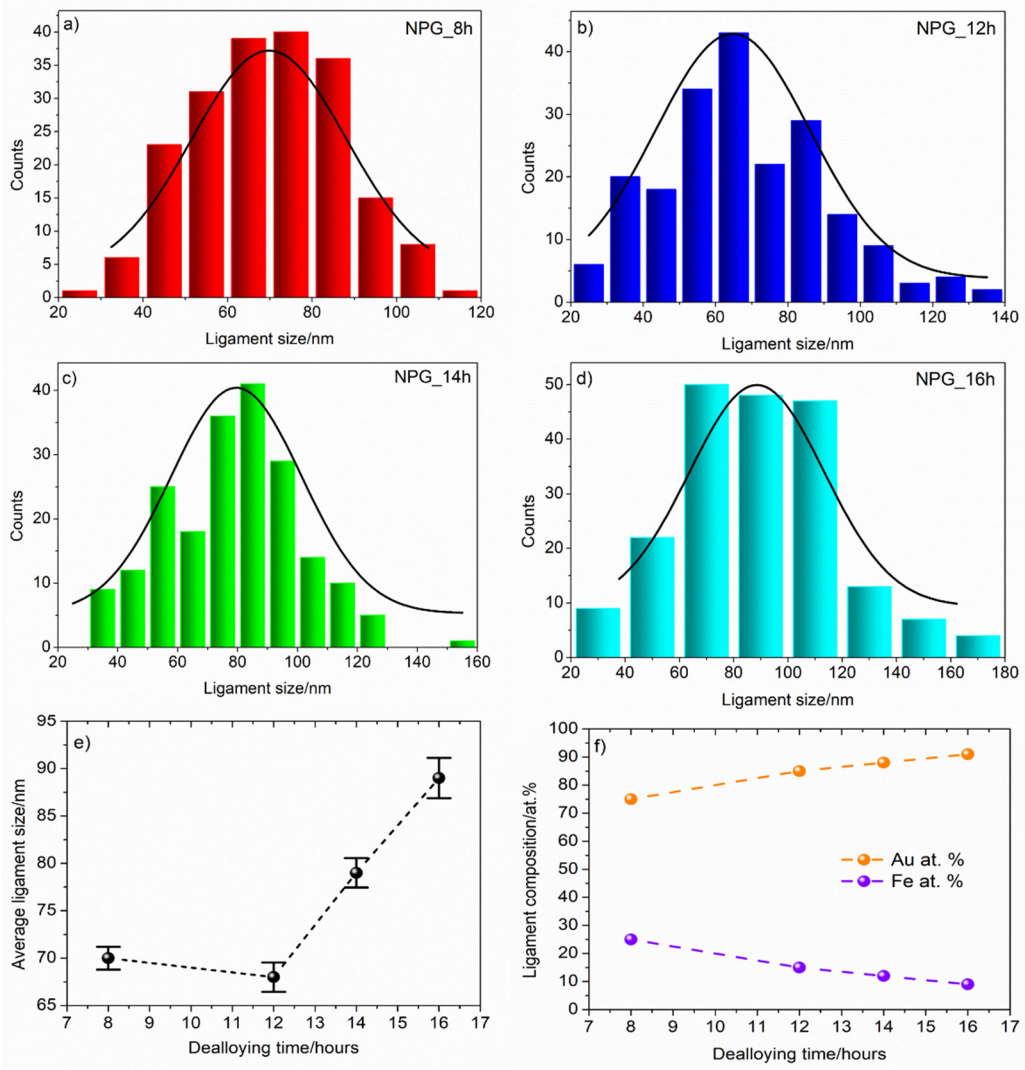

Figure 4. Statistical and compositional analyses of ligaments: histograms and distributions for the samples (**a**) NPG_8h, (**b**) NPG_12h, (**c**) NPG_14h, and (**d**) NPG_16h. (**e**) Average ligament size within standard error as a function of dealloying time. (**f**) EDS analysis of ligaments; the dashed lines have to be intended as a guide for the eyes.

From the morphological point of view, the ligaments obtained from dealloying of $Au_{33}Fe_{67}$ metastable supersaturated solid solution show a smooth appearance, which is typical of NPGs synthesized from crystalline precursors [10], independent of the elements coupled with Au. The dimension of ligaments depends on the starting concentration of Au, which must be within the parting limit, and the condition of dealloying mentioned above in the introduction.

3.3. Electrochemical Behavior in Basic Solution

In the literature, it is reported that the Brunauer–Emmett–Teller (BET) method of surface area determination gives the specific surface area for an NPG with similar Au

content in the range of 6.4 to 10 m^2 g^{-1} [10,43–45]. Although it is a reliable method, it is limited in terms of the amount of NPG sample required for the measurement. As Detsi et al. pointed out, each BET measurement requires at least 250 mg of NPG for reliable surface area evaluation [43], essentially amounting to a total of 1 g of NPG for the four samples investigated, which is an excessive amount of material. On the contrary, only a few milligrams of material are commonly used for experiments on nanoporous metals [46–51]. For this reason, we opted for the electrochemical method of surface area determination.

Electrochemical characterization of the as-dealloyed NPGs was performed by subjecting samples to cyclic voltammetry (CV) scans in 0.5 M KOH as provided in Figure 5a; NPG_8h was discarded for the electrochemical and methanol electro-oxidation tests because of the higher amount of iron in the ligaments. The obtained curve reflects the occurrence of various processes on the surface of the sample on account of their composition and microstructure. While forward scan is underway, OH^- ions are chemisorbed on the sample surface, in the non-faradaic potential range, resulting in the creation of a layer of hydroxy intermediate, Au-$OH^{(1-\lambda)-}$, where λ stands for the charge transfer coefficient. This intermediate layer is then utilized in the formation of Au oxides [5,7], marked by the current peak at around 0.29 V. The backward scans show the peak at 0.1 V obtained as a result of the reduction of Au oxides. The position of this reduction peak is hardly changed in the second cycle, proving the stability of the electrode. The EASA of the three samples was measured using the procedure mentioned in Section 2 previously. Figure 5b depicts the calculated EASA for each of the three samples. In addition to having the highest EASA, NPG_16h has the highest dealloyed volume credited to 16 h of dealloying, as reported in previous works [52]. Thus, it must show the highest current density of methanol electro-oxidation weighed up to the other samples [52]. For these reasons, NPG_16h was the sample of choice for the methanol electro-oxidation studies.

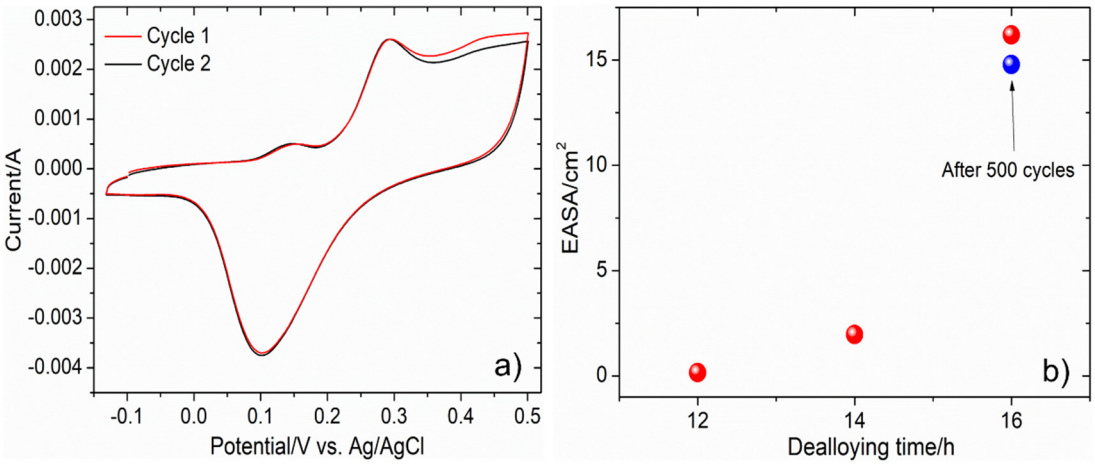

Figure 5. (**a**) CV scans of NPG_16h in the potential range of −0.13 to 0.5 vs. Ag/AgCl in 0.5 M KOH solution. (**b**) EASA of NPG_12h, NPG_14h, and NPG_16h denoted by red dots before methanol electro-oxidation and EASA of NPG_16h denoted by a blue dot after 500 CV scan cycles of methanol electro-oxidation.

3.4. Methanol Electro-Oxidation Behavior

The nanoporous structure of the sample allows for facile electro-oxidation of methanol by virtue of its high number of active sites in the form of low-coordinated Au sites, such as step, edge, or kink sites along with the structural defects [53]. As shown in the above section, NPG_16h shows the highest EASA, and thus, it was selected as electrode for the electrocatalytic test of methanol oxidation in basic solutions: 500 cycles of CV scan for NPG_16h are presented in Figure 6.

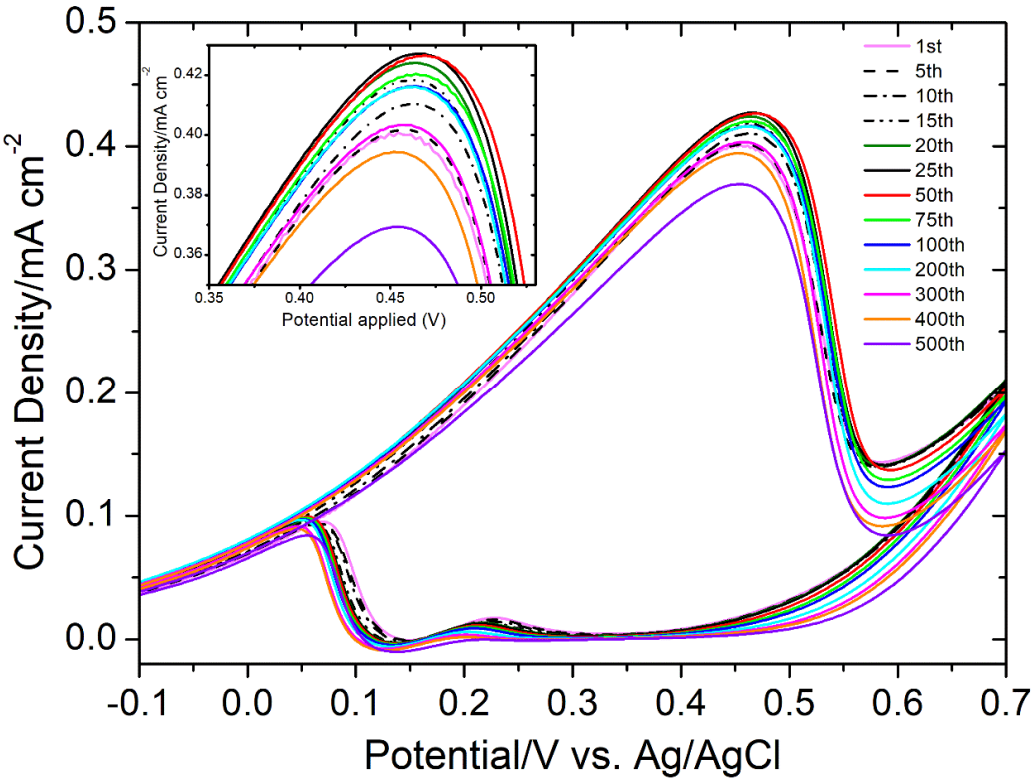

Figure 6. CV curves of NPG_16h for 500 scan cycles in a solution of 5 M CH_3OH in 0.5 M KOH at a scan rate of 20 mV/s. The inset gives a magnified look at the potential range, peak potential, and peak current density of methanol electro-oxidation.

As mentioned previously, during the positive scan and at the onset of the current peak, the formation of a layer of pre-oxidized species, such as Au-$OH^{(1-\lambda)-}$, takes place owing to chemisorption of OH^- ions on the sample surface. This intermediate layer of Au-$OH^{(1-\lambda)-}$ reacts with methanol present in the solution and oxidizes it to form ions with the exchange of four electrons according to the reaction below [5,10,16]:

$$CH_3OH + 5OH^- \rightarrow HCOO^- + 4H_2O + 4e^- \quad (1)$$

The current density at the peak maximum increases cycle by cycle up to the 25th of forward scan. This trend is an indicator of gradual increment in the electrochemical activity of the sample; as reported elsewhere [27], the increment of the current density might be ascribed to a higher rate of methanol oxidation reached during the process up to the 25th cycle with an increasing efficiency of recovery of the electrode surface. During the next cycles, the intensity of the process slightly declines probably due to some changes in the surface and/or poisoning effect. With respect to the 25th cycle, methanol electro-oxidation occurs in the potential range of 0.35 to 0.55 V vs. Ag/AgCl. Neat peaks of anodic current corresponding to reaction (1) can be observed in the inset of Figure 6 with maxima at the potential of 0.47 V vs. Ag/AgCl. After the 25th cycle, a decline in current density ensues until the last cycle. This pattern can be linked to the progressive consumption of the Au-$OH^{(1-\lambda)-}$ species in the formation of Au oxides [5,16,17]. This affects the number of exposed active Au sites sufficiently enough so as to negatively impact the current density after the 25th cycle. However, at the same time, this drop in current density from 0.43 to 0.37 mA/cm^2 is only by 0.06 mA/cm^2, which is not drastic. It indicates that the sample is exceedingly stable, retaining its electrochemical activity even after 500 CV cycles with a minute drop in current density.

When the potential is swept in the backward scan direction, the oxidation of methanol is resumed according to reaction (1) in the same potential range where Au oxides are

reduced (from 0.25 V to −0.05 V), represented by the reappearance of current peak. The current density demonstrated by this peak augments from the 1st cycle up to the 25th and then faces a steady decay up to the last cycle (i.e., 500th cycle). This trend can also be associated with the same reason as for the forward scan. The greater is the methanol electro-oxidation, the higher is the current density.

The poisoning tolerance of electrocatalysts in DMFCs can be evaluated by finding the peak current ratio of the forward-to-reverse scans (I_f/I_r) [26,54]. Generally, the higher is the I_f/I_r ratio, the better is the resistance to electrode poisoning from carbonaceous species [26]. A commercial Pt/C electrocatalyst has a poisoning tolerance of 2.3, while NPG_16h in this case has a tolerance of 4.35 [26]. This adds to the overall favorable properties of the NPG_16h sample as a superb alternative for methanol electro-oxidation.

Figure 7a provides a look at the electrochemical stability of the sample, where the current density (on the right axis) and peak potential (on the left axis) at the maximum of the CV scan vs. the number of cycles is presented. The current density is normalized with respect to the maximum value recorded in the first cycle [7]. The sample shows remarkable stability after 500 cycles with the efficiency of current density down to only 86%. The peak potential also remains quite steady in the potential range of 0.47 to 0.45 V for all the 500 cycles. Figure 7b contains the graph of the current density normalized with respect to the 25th cycle vs. the number of CV cycles. The maximum of the current density of the 25th cycle is considered the standard 100% here as it is the highest current density observed, and the rest are normalized accordingly. As reported in the literature [27], the electrochemical performance of the sample decreases gradually because of coverage of active sites by oxides and other chemical species.

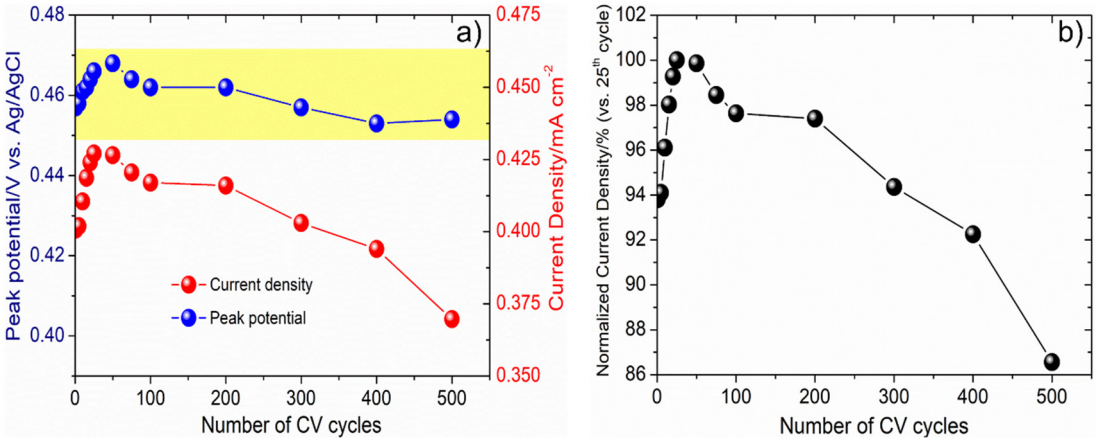

Figure 7. Graph depicting the stability of NPG_16h up to 500 CV cycles in terms of (**a**) the peak potential (*y*-axis on the left) and current density at the peak potential (*y*-axis on the right) and (**b**) peak current density of methanol electro-oxidation normalized with respect to the 25th cycle.

After 500 cycles, the sample was reactivated by immersing in concentrated HNO_3 for 15 min. The EASA of NPG_16h was measured again after the 500 cycles of CV scan following the same procedure, as reported earlier in Section 2. The comparison of the EASAs of NPG_16h before and after the 500 cycles of CV scan is displayed in Figure 5b in the form of red and blue dots, respectively. It is clear that there is only a minor decrement in the EASA, which denotes remarkable electrocatalytic capacity, stability, and longevity of the tested sample. The performance of NPG_16h in this work is compared with those of several contemporary samples reported in the literature, in terms of peak potentials of methanol oxidation and corresponding current density, in Table 1.

Despite the huge number of data reported in the literature, due to the increasing interest in this field of research, it is difficult to clearly compare different samples; the main issue is the inhomogeneity in the procedure followed for the electrochemical tests (i.e., different type of electrolyte in terms of basic or acid conditions, concentration of

methanol, different scan rate, and current data reported as values of current density or simply current but without mentioning the EASA). A fair comparison, however, might be conducted among NPGs synthesized from different precursors: NPGs from Ag–Au crystalline precursors [55] show peak potentials, converted in Ag/AgCl, similar to our samples but current densities three orders of magnitude smaller compared with NPG_16h. Among NPGs synthesized from amorphous precursors by our group of research [33], the fully dealloyed sample exhibits a lower peak potential of 0.22 V and a higher current density of 0.68 mA/cm^2.

NPG_16h represents a valid alternative to substitute NPGs from Ag–Au alloys showing better catalytic properties in terms of current density and peak potential, which promotes avoidance of Ag, an expensive element in the list of critical raw materials [56], and usage of the more abundant and affordable Fe instead.

Table 1. Comparison of our work with the literature in terms of peak potentials of methanol oxidation and peak current/current density.

Sample	Electrolyte	Scan Rate (mV/s)	Peak Oxidation Voltage	Peak Oxidation Current/Current Density	Ref.
NPG_16h	5 M CH_3OH in 0.5 M KOH	20	0.47 V Ag/AgCl	0.43 mA/cm^2	This work
NPG-A from Au–Ag (data)	1 M KOH + 1 M CH_3OH	10	0.550 V Hg/Hg_2SO_4 0.491 Ag/AgCl	42.0 µA/cm^2	[55]
NPG-B from Au–Ag	1 M KOH + 1 M CH_3OH	10	0.532 V Hg/Hg_2SO_4 0.473 Ag/AgCl	101.1 µA/cm^2	[55]
NPG-C from Au–Ag	1 M KOH + 1 M CH_3OH	10	0.420 V Hg/Hg_2SO_4 0.361 Ag/AgCl	119.4 µA/cm^2	[55]
NPG_6h	5 M CH_3OH in 0.5 M KOH	20	0.22 V Ag/AgCl	0.68 mA/cm^2	[33]
Rh-NSs/RGO hybrids	1 M CH_3OH in 1 M KOH	50	0.61 V Ag/AgCl	0.52 mA/cm^2	[26]
EC/rGO/NiOOH	0.01 M CH_3OH in 0.1 M NaOH	50	0.66 V vs. Ag/AgCl	0.75 mA	[57]
EC/rGO/NiOOH-FeOOH	0.01 M CH_3OH in 0.1 M NaOH	50	0.57 V vs. Ag/AgCl	0.8 mA	[57]
Ni–Pt/carbon paper electrode	1 M CH_3OH in 0.5 M KOH	20	−0.2 V vs. Ag/AgCl	1.8 mA	[58]
Pt_3Ni nanoparticles	1 M CH_3OH in 0.1 M $HClO_4$	50	1.04 V vs. RHE	0.5 mA/cm^2	[59]
Pt/CNTs-80	0.5 M CH_3OH In 0.5 M H_2SO_4	50	0.69 V vs. Ag/AgCl	1.83 mA/cm^2	[60]
Pd-Ir-O/NGS	1 M CH_3OH in 1 M KOH	50	0.81 V vs. RHE	3.26 mA cm^{-2}	[61]
$MnCo_2O_4$	0.5 M CH_3OH in 1 M KOH	10	0.7 V vs. Ag/AgCl	95 A/g	[62]
$Mn_{0.6}Zn_{0.4}Co_2O_4$/rGO	0.5 M CH_3OH in 1 M KOH	50	0.8 V vs. Ag/AgCl	142.3 mA/cm^2	[63]
Pt/MnO2/Rgo	0.5 M CH_3OH in 0.5 M H_2SO_4	50	0.9 V vs. RHE	23 mA/cm^2	[54]
Pt/RuO_2/CNT	1 M CH_3OH in 1 M $HClO_4$	-	0.74 V vs. Ag/AgCl	609 A/g Pt	[29]
Pt/RuO_2/TiO_2-NTs	0.5 M CH_3OH in 1 M H_2SO_4	0.5	0.8 V	100 mA/cm^2	[64]
C/CoAg	1 M CH_3OH in 0.1 M KOH	50	0.48 V	2.30 A/g C	[65]
C/Co	1 M CH_3OH in 0.1 M KOH	50	0.58 V	0.35 A/g C	[65]
RuO_2/$MnCo_2O_4$/rGO	0.5 M CH_3OH in 1 M KOH	20	0.5 V vs Ag/AgCl	20.44 mA/cm^2	[66]
Pt/p-MDAB/CF	1 M CH_3OH in 0.5 M H_2SO_4	50	0.71 V vs Ag/AgCl	405 mA mg^{-1} Pt	[67]
Ni/ZMCPE	0.1 M CH_3OH in 0.1 M NaOH	20	0.68 V vs. Ag/AgCl	0.85 mA	[68]
13XPtRu	0.5 M CH_3OH in 0.5 M NaOH	20	−0.23 V vs. Ag/AgCl	0.56 mA	[69]
RGO/bimetallic Pt–Pd alloy/CeO_2	1 M CH_3OH in 0.5 M H_2SO_4	50	0.8 V vs. Ag/AgCl	69.82 mA cm^2	[70]
Pt/BNC NTs	1 M CH_3OH in 0.5 M H_2SO_4	50	0.73 V vs. Ag/AgCl	0.73 A mg^{-1} Pt	[71]

4. Conclusions

A cheap Fe-rich $Au_{33}Fe_{67}$ precursor was used to fabricate nanoporous gold successfully. Arc-melting and melt-spinning techniques were employed subsequently to form homogenous and long ribbons of the precursor. Afterwards, the as-quenched ribbons were chemically dealloyed in 1 M HCl at 70 °C for different spans of time with each as-prepared NPG sample showcasing well-defined nanoporous morphology. The samples exhibited few noticeable trends (i.e., increased dealloying time induced an enhancement in (i) the homogeneity of the surface morphology, (ii) the ligament size, and (iii) the atomic percentage of Au). The NPG sample with the highest surface area was put to test as an electrocatalyst for methanol electro-oxidation. The sample performed excellently in a basic solution of methanol and KOH, demonstrating a low peak potential of −0.47 V vs. Ag/AgCl along with a high current density of 0.43 mA/cm^2 at the oxidation peak potential. The same sample also displayed impressive stability with a minor drop in the current density and high poisoning tolerance. Quite importantly, an easy and rapid dealloying procedure was employed using a cheap and abundant Fe precursor and by avoiding the use of critical raw materials to fabricate an efficient and sustainable alternative for methanol electro-oxidation in the form of the nanoporous gold sample, NPG_16h.

Supplementary Materials: The following supporting information can be downloaded at: https://www.mdpi.com/article/10.3390/coatings12060831/s1: Figure S1: SEM-SE cross-sectional images of (a) NPG_8h, (b) NPG_12h, (c) NPG_14h and (d) NPG_16h with the insets showing magnified view of respective samples.

Author Contributions: Conceptualization, D.R., F.S. and P.R.; data curation, D.R. and F.S.; formal analysis, D.R., F.S. and P.R.; funding acquisition, P.R.; investigation, D.R., F.S. and G.F.; methodology, D.R., F.S. and G.F.; project administration, P.R.; resources, P.R.; supervision, F.S. and P.R.; validation, F.S. and P.R.; visualization, D.R., F.S. and P.R.; writing—original draft, D.R.; writing—review and editing, D.R., F.S. and P.R. All authors have read and agreed to the published version of the manuscript.

Funding: This research was funded by Compagnia di San Paolo-Bando ex-post-Anno 2018.

Institutional Review Board Statement: Not applicable.

Informed Consent Statement: Not applicable.

Data Availability Statement: Data will be made available on request.

Acknowledgments: Acquisition of the SEM images has been performed thanks to NanoFacility Piemonte, INRIM.

Conflicts of Interest: The authors declare no conflict of interest.

References

1. McCue, I.; Benn, E.; Gaskey, B.; Erlebacher, J. Dealloying and Dealloyed Materials. *Annu. Rev. Mater. Res.* **2016**, *46*, 263–286. [CrossRef]
2. Xue, Y.; Scaglione, F.; Rizzi, P.; Battezzati, L.; Denis, P.; Fecht, H.-J. Electrodeposited platinum on de-alloyed nanoporous gold with enhanced electro-catalytic performance. *Appl. Surf. Sci.* **2019**, *476*, 412–417. [CrossRef]
3. Xue, Y.; Wang, S.; Shi, P.; Huang, Y.; Scaglione, F.; Rizzi, P.; Battezzati, L.; Denis, P.; Fecht, H.J. Nanoporous gold chemically de-alloyed from Au-based amorphous thin film for electrochemical nonenzymatic H_2O_2 sensing. *Chem. Phys. Lett.* **2019**, *723*, 22–27. [CrossRef]
4. Xiao, S.; Wang, S.; Wang, X.; Xu, P. Nanoporous gold: A review and potentials in biotechnological and biomedical applications. *Nano Sel.* **2021**, *2*, 1437–1458. [CrossRef]
5. Mohan, K.; Shahane, N.; Liu, R.; Smet, V.; Antoniou, A. A Review of Nanoporous Metals in Interconnects. *JOM* **2018**, *70*, 2192–2204. [CrossRef]
6. Kim, S.H. Nanoporous Gold for Energy Applications. *Chem. Rec.* **2021**, *21*, 1199–1215. [CrossRef]
7. Kim, S.H. Nanoporous gold: Preparation and applications to catalysis and sensors. *Curr. Appl. Phys.* **2018**, *18*, 810–818. [CrossRef]
8. Scaglione, F.; Gebert, A.; Battezzati, L. Dealloying of an Au-based amorphous alloy. *Intermetallics* **2010**, *18*, 2338–2342. [CrossRef]
9. Scaglione, F.; Xue, Y.; Celegato, F.; Rizzi, P.; Battezzati, L. Amorphous molybdenum sulphide @ nanoporous gold as catalyst for hydrogen evolution reaction in acidic environment. *J. Mater. Sci.* **2018**, *53*, 12388–12398. [CrossRef]

10. Scaglione, F.; Celegato, F.; Rizzi, P.; Battezzati, L. A comparison of de-alloying crystalline and amorphous multicomponent Au alloys. *Intermetallics* **2015**, *66*, 82–87. [CrossRef]
11. Scaglione, F.; Rizzi, P.; Battezzati, L. De-alloying kinetics of an Au-based amorphous alloys. *J. Alloys Compd.* **2012**, *536*, S60–S64. [CrossRef]
12. Rizzi, P.; Scaglione, F.; Battezzati, L. Nanoporous gold by dealloying of an amorphous precursor. *J. Alloys Compd.* **2014**, *586*, S117–S120. [CrossRef]
13. Van Petegem, S.; Brandstetter, S.; Maass, R.; Hodge, A.M.; El-Dasher, B.S.; Biener, J.; Schmitt, B.; Borca, C.; Swygenhoven, H. Van On the Microstructure of Nanoporous Gold: An X-ray Diffraction Study. *Nano Lett.* **2009**, *9*, 1158–1163. [CrossRef]
14. He, Z.; Huang, Y.; He, F. Preparation of nanoporous molybdenum film by dealloying an immiscible Mo–Zn system for hydrogen evolution reaction. *RSC Adv.* **2016**, *6*, 15390–15393. [CrossRef]
15. Li, X.; Chen, Q.; McCue, I.; Snyder, J.; Crozier, P.; Erlebacher, J.; Sieradzki, K. Dealloying of Noble-Metal Alloy Nanoparticles. *Nano Lett.* **2014**, *14*, 2569–2577. [CrossRef] [PubMed]
16. Paschalidou, E.M.; Fiore, G.; Xue, Y.; Scaglione, F.; Celegato, F.; Gebert, A.; Oswald, S.; Wolff, U.; Rizzi, P.; Battezzati, L. Comparing selective corrosion of Au-based amorphous, partially amorphous, and devitrified alloys. *J. Alloys Compd.* **2018**, *745*, 212–216. [CrossRef]
17. Xue, Y.; Scaglione, F.; Rizzi, P.; Battezzati, L. Improving the chemical de-alloying of amorphous Au alloys. *Corros. Sci.* **2017**, *127*, 141–146. [CrossRef]
18. Xue, Y.; Scaglione, F.; Celegato, F.; Denis, P.; Fecht, H.-J.; Rizzi, P.; Battezzati, L. Shape controlled gold nanostructures on de-alloyed nanoporous gold with excellent SERS performance. *Chem. Phys. Lett.* **2018**, *709*, 46–51. [CrossRef]
19. The Materials Information Society. *ASM Handbook Volume 3—Alloy Phase Diagrams*; The Materials Information Society: Materials Park, OH, USA, 1992. [CrossRef]
20. Alaba, P.A.; Lee, C.S.; Abnisa, F.; Aroua, M.K.; Cognet, P.; Pérès, Y.; Wan Daud, W.M.A. A review of recent progress on electrocatalysts toward efficient glycerol electrooxidation. *Rev. Chem. Eng.* **2020**, *36*, 779–811. [CrossRef]
21. Houache, M.S.E.; Cossar, E.; Ntais, S.; Baranova, E.A. Electrochemical modification of nickel surfaces for efficient glycerol electrooxidation. *J. Power Sources* **2018**, *375*, 310–319. [CrossRef]
22. Vaishnavi, B.J.; Sujith, S.; Kulal, N.; Manjunathan, P.; Shanbhag, G.V. Utilization of renewable resources: Investigation on role of active sites in zeolite catalyst for transformation of furfuryl alcohol into alkyl levulinate. *Mol. Catal.* **2021**, *502*, 111361. [CrossRef]
23. Venkateswarlu, K. *Ashes from Organic Waste as Reagents in Synthetic Chemistry: A Review*; Springer International Publishing: Berlin/Heidelberg, Germany, 2021; Volume 19, ISBN 0123456789.
24. Cruz-Navarro, J.A.; Mendoza-Huizar, L.H.; Salazar-Pereda, V.; Cobos-Murcia, J.Á.; Colorado-Peralta, R.; Álvarez-Romero, G.A. Progress in the use of electrodes modified with coordination compounds for methanol electro-oxidation. *Inorg. Chim. Acta* **2021**, *520*, 120293. [CrossRef]
25. Valter, M.; Wickman, B.; Hellman, A. Solvent Effects for Methanol Electrooxidation on Gold. *J. Phys. Chem. C* **2021**, *125*, 1355–1360. [CrossRef]
26. Kang, Y.; Xue, Q.; Jin, P.; Jiang, J.; Zeng, J.; Chen, Y. Rhodium Nanosheets–Reduced Graphene Oxide Hybrids: A Highly Active Platinum-Alternative Electrocatalyst for the Methanol Oxidation Reaction in Alkaline Media. *ACS Sustain. Chem. Eng.* **2017**, *5*, 10156–10162. [CrossRef]
27. Krawczyk, P.; Rozmanowski, T.; Frankowski, M. Methanol Electrooxidation at Electrodes Made of Exfoliated Graphite/Nickel/Palladium Composite. *Catal. Lett.* **2019**, *149*, 2307–2316. [CrossRef]
28. Tritsaris, G.A.; Rossmeisl, J. Methanol oxidation on model elemental and bimetallic transition metal surfaces. *J. Phys. Chem. C* **2012**, *116*, 11980–11986. [CrossRef]
29. Peng, F.; Zhou, C.; Wang, H.; Yu, H.; Liang, J.; Yang, J. The role of RuO_2 in the electrocatalytic oxidation of methanol for direct methanol fuel cell. *Catal. Commun.* **2009**, *10*, 533–537. [CrossRef]
30. Nagavolu, C.; Susmitha, K.; Raghavender, M.; Giribabu, L.; Bhanu Sankara Rao, K.; Smith, C.T.G.; Mills, C.A.; Silva, S.R.P.; Srikanth, V.V.S.S. Pt-free spray coated reduced graphene oxide counter electrodes for dye sensitized solar cells. *Sol. Energy* **2016**, *137*, 143–147. [CrossRef]
31. Gurulakshmi, M.; Meenakshamma, A.; Susmitha, K.; Charanadhar, N.; Srikanth, V.V.S.S.; Narendra Babu, S.; Venkata Subbaiah, Y.P.; Venkateswarlu, K.; Raghavender, M. A transparent and Pt-free all-carbon nanocomposite counter electrode catalyst for efficient dye sensitized solar cells. *Sol. Energy* **2019**, *193*, 568–575. [CrossRef]
32. Dong, B.; Li, W.; Huang, X.; Ali, Z.; Zhang, T.; Yang, Z.; Hou, Y. Fabrication of hierarchical hollow Mn doped $Ni(OH)_2$ nanostructures with enhanced catalytic activity towards electrochemical oxidation of methanol. *Nano Energy* **2019**, *55*, 37–41. [CrossRef]
33. Remmel, A.L.; Ratso, S.; Divitini, G.; Danilson, M.; Mikli, V.; Uibu, M.; Aruväli, J.; Kruusenberg, I. Nickel and Nitrogen-Doped Bifunctional ORR and HER Electrocatalysts Derived from CO_2. *ACS Sustain. Chem. Eng.* **2022**, *10*, 134–145. [CrossRef]
34. Rezaee, S.; Shahrokhian, S. Facile synthesis of petal-like NiCo/NiO-CoO/nanoporous carbon composite based on mixed-metallic MOFs and their application for electrocatalytic oxidation of methanol. *Appl. Catal. B Environ.* **2019**, *244*, 802–813. [CrossRef]
35. Raj, D.; Scaglione, F.; Fiore, G.; Celegato, F.; Rizzi, P. Nanostructured molybdenum oxides from aluminium-based intermetallic compound: Synthesis and application in hydrogen evolution reaction. *Nanomaterials* **2021**, *11*, 1313. [CrossRef] [PubMed]

36. Zhang, Z.; Wang, Y.; Wang, Y.; Wang, X.; Qi, Z.; Ji, H.; Zhao, C. Formation of ultrafine nanoporous gold related to surface diffusion of gold adatoms during dealloying of Al_2Au in an alkaline solution. *Scr. Mater.* **2010**, *62*, 137–140. [CrossRef]
37. Machado, S.A.S.; Avaca, L.A. The hydrogen evolution reaction on nickel surfaces stabilized by H-absorption. *Electrochim. Acta* **1994**, *39*, 1385–1391. [CrossRef]
38. Ahn, S.H.; Hwang, S.J.; Yoo, S.J.; Choi, I.; Kim, H.-J.; Jang, J.H.; Nam, S.W.; Lim, T.-H.; Lim, T.; Kim, S.-K.; et al. Electrodeposited Ni dendrites with high activity and durability for hydrogen evolution reaction in alkaline water electrolysis. *J. Mater. Chem.* **2012**, *22*, 15153–15159. [CrossRef]
39. Lukaszewski, M.; Soszko, M.; Czerwiński, A. Electrochemical methods of real surface area determination of noble metal electrodes—An overview. *Int. J. Electrochem. Sci.* **2016**, *11*, 4442–4469. [CrossRef]
40. Ogihara, H.; Fujii, M.; Saji, T. Hydrogen evolution reaction (HER) over electroless-deposited nickel nanospike arrays. *RSC Adv.* **2014**, *4*, 58660–58663. [CrossRef]
41. Favez, D.; Wagnière, J.D.; Rappaz, M. Au-Fe alloy solidification and solid-state transformations. *Acta Mater.* **2010**, *58*, 1016–1025. [CrossRef]
42. Kumar, P.S.M.; Sivakumar, T.; Fujita, T.; Jayavel, R.; Abe, H. Synthesis of metastable Au-Fe alloy using ordered nanoporous silica as a hard template. *Metals* **2018**, *8*, 17. [CrossRef]
43. Detsi, E.; De Jong, E.; Zinchenko, A.; Vuković, Z.; Vuković, I.; Punzhin, S.; Loos, K.; Ten Brinke, G.; De Raedt, H.A.; Onck, P.R.; et al. On the specific surface area of nanoporous materials. *Acta Mater.* **2011**, *59*, 7488–7497. [CrossRef]
44. Ji, C.; Searson, P.C. Synthesis and characterization of nanoporous gold nanowires. *J. Phys. Chem. B* **2003**, *107*, 4494–4499. [CrossRef]
45. Tan, Y.H.; Davis, J.A.; Fujikawa, K.; Ganesh, N.V.; Demchenko, A.V.; Stine, K.J. Surface area and pore size characteristics of nanoporous gold subjected to thermal, mechanical, or surface modification studied using gas adsorption isotherms, cyclic voltammetry, thermogravimetric analysis, and scanning electron microscopy. *J. Mater. Chem.* **2012**, *22*, 6733–6745. [CrossRef]
46. Wittstock, A.; Zielasek, V.; Biener, J.; Friend, C.M.; Bäumer, M. Nanoporous Gold Catalysts for Selective Gas-Phase Oxidative Coupling of Methanol at Low Temperature. *Science* **2010**, *327*, 319–322. [CrossRef]
47. Lang, X.Y.; Yuan, H.T.; Iwasa, Y.; Chen, M.W. Three-dimensional nanoporous gold for electrochemical supercapacitors. *Scr. Mater.* **2011**, *64*, 923–926. [CrossRef]
48. Weissmüller, J.; Viswanath, R.N.; Kramer, D.; Zimmer, P.; Würschum, R.; Gleiter, H. Charge-induced reversible strain in a metal. *Science* **2003**, *300*, 312–315. [CrossRef]
49. Jin, H.J.; Wang, X.L.; Parida, S.; Wang, K.; Seo, M.; Weissmüller, J. Nanoporous au-pt alloys as large strain electrochemical actuators. *Nano Lett.* **2010**, *10*, 187–194. [CrossRef]
50. Biener, J.; Wittstock, A.; Zepeda-Ruiz, L.A.; Biener, M.M.; Zielasek, V.; Kramer, D.; Viswanath, R.N.; Weissmüller, J.; Bäumer, M.; Hamza, A.V. Surface-chemistry-driven actuation in nanoporous gold. *Nat. Mater.* **2009**, *8*, 47–51. [CrossRef]
51. Detsi, E.; van de Schootbrugge, M.; Punzhin, S.; Onck, P.R.; De Hosson, J.T.M. On tuning the morphology of nanoporous gold. *Scr. Mater.* **2011**, *64*, 319–322. [CrossRef]
52. Paschalidou, E.M.; Scaglione, F.; Gebert, A.; Oswald, S.; Rizzi, P.; Battezzati, L. Partially and fully de-alloyed glassy ribbons based on Au: Application in methanol electro-oxidation studies. *J. Alloys Compd.* **2016**, *667*, 302–309. [CrossRef]
53. Gonçalves, J.M.; Kumar, A.; da Silva, M.I.; Toma, H.E.; Martins, P.R.; Araki, K.; Bertotti, M.; Angnes, L. Nanoporous Gold-Based Materials for Electrochemical Energy Storage and Conversion. *Energy Technol.* **2021**, *9*, 2000927. [CrossRef]
54. Yuan, W.; Zhang, Y.; Zhang, N.; Yin, C.; Zhang, X.; Liu, X. Carbon riveted Pt-MnO2/reduced graphene oxide anode catalyst for DMFC. *Catal. Commun.* **2017**, *100*, 66–70. [CrossRef]
55. Graf, M.; Haensch, M.; Carstens, J.; Wittstock, G.; Weissmüller, J. Electrocatalytic methanol oxidation with nanoporous gold: Microstructure and selectivity. *Nanoscale* **2017**, *9*, 17839–17848. [CrossRef] [PubMed]
56. Blengini, G.A.; Latunussa, C.E.L.; Eynard, U.; Torres de Matos, C.; Wittmer, D.; Georgitzikis, K.; Pavel, C.; Carrara, S.; Mancini, L.; Unguru, M.; et al. *Study on the EU's List of Critical Raw Materials (2020) Final Report*; Publications Office of the European Union: Luxembourg, 2020.
57. de Oliveira, J.P.J.; de Sá, A.C.; Paim, L.L. Electrocatalysis of Ethanol and Methanol Electrooxidation by Composite Electrodes with NiOOH/FeOOH Supported on Reduced Graphene Oxide onto Composite Electrodes. *Chem. Proc.* **2020**, *2*, 2. [CrossRef]
58. Abdullah Mirzaie, R.; Eshghi, A. Study of methanol electro-oxidation on Ni and Ni–Pt/carbon paper electrodes for direct methanol fuel cell applications. *Surf. Eng.* **2014**, *30*, 263–267. [CrossRef]
59. Chen, S.; Wu, H.; Tao, J.; Xin, H.; Zhu, Y.; Chen, J. Pt–Ni Seed-Core-Frame Hierarchical Nanostructures and Their Conversion to Nanoframes for Enhanced Methanol Electro-Oxidation. *Catalysts* **2019**, *9*, 39. [CrossRef]
60. Yang, P.; Zhou, Z.; Zheng, T.; Gu, C.; Gong, X.; Zhang, Y.; Xie, Y.; Yang, N.; Fei, J. A novel strategy to synthesize Pt/CNTs nanocatalyst with highly improved activity for methanol electrooxidation. *J. Electroanal. Chem.* **2021**, *897*, 115557. [CrossRef]
61. Shu, J.; Li, R.; Lian, Z.; Zhang, W.; Jin, R.; Yang, H.; Li, S. In-situ oxidation of Palladium–Iridium nanoalloy anchored on Nitrogen-doped graphene as an efficient catalyst for methanol electrooxidation. *J. Colloid Interface Sci.* **2022**, *605*, 44–53. [CrossRef]
62. Thorat, G.M.; Jadhav, H.S.; Seo, J.G. Bi-functionality of mesostructured $MnCo_2O_4$ microspheres for supercapacitor and methanol electro-oxidation. *Ceram. Int.* **2017**, *43*, 2670–2679. [CrossRef]

63. Rebekah, A.; Anantharaj, S.; Viswanthan, C.; Ponpandian, N. Zn-substituted $MnCo_2O_4$ nanostructure anchored over rGO for boosting the electrocatalytic performance towards methanol oxidation and oxygen evolution reaction (OER). *Int. J. Hydrogen Energy* **2020**, *45*, 14713–14727. [CrossRef]
64. Zheng, J.; Huang, K.; Hou, G.; Zhang, H.; Cao, H. A highly active Pt nanocatalysts supported on RuO_2 modified TiO_2-NTs for methanol electrooxidation with excellent CO tolerance. *Int. J. Hydrogen Energy* **2019**, *44*, 31506–31514. [CrossRef]
65. Şahin, E.A.; Solmaz, R. Methanol electrooxidation activity of binary CoAg electrocatalyst. *Int. J. Hydrogen Energy* **2020**, *45*, 35013–35022. [CrossRef]
66. Askari, M.B.; Rozati, S.M.; Salarizadeh, P.; Saeidfirozeh, H.; Di Bartolomeo, A. A remarkable three-component RuO_2-$MnCo_2O_4$/rGO nanocatalyst towards methanol electrooxidation. *Int. J. Hydrogen Energy* **2021**, *46*, 36792–36800. [CrossRef]
67. Kamyabi, M.A.; Ebrahimi Qaratapeh, K.; Jadali, S.; Moharramnezhad, M. Decorating the carbon felt electrode with polymeric platinize nanocomposite: Characterization and electrocatalytic activity towards methanol oxidation reaction. *J. Chem. Sci.* **2019**, *131*, 61. [CrossRef]
68. Raoof, J.B.; Azizi, N.; Ojani, R.; Ghodrati, S.; Abrishamkar, M.; Chekin, F. Synthesis of ZSM-5 zeolite: Electrochemical behavior of carbon paste electrode modified with Ni (II)-zeolite and its application for electrocatalytic oxidation of methanol. *Int. J. Hydrogen Energy* **2011**, *36*, 13295–13300. [CrossRef]
69. Mojović, Z.; Mudrinić, T.; Rabi-Stankovic, A.; Ivanovic-Sasic, A.; Marinovic, S.; Žunić, M.; Jovanović, D. Methanol Electrooxidation on PtRu Modified Zeolite X. *Sci. Sinter.* **2013**, *45*, 89–96. [CrossRef]
70. Hanifah, M.F.R.; Jaafar, J.; Othman, M.H.D.; Ismail, A.F.; Rahman, M.A.; Yusof, N.; Salleh, W.N.W.; Aziz, F.; Abdul Ajid, A.Z. Advanced ternary RGO/bimetallic Pt-Pd alloy/CeO_2 nanocomposite electrocatalyst by one-step hydrothermal-assisted formic acid reduction reaction for methanol electrooxidation. *J. Environ. Chem. Eng.* **2021**, *9*, 104991. [CrossRef]
71. Zhou, Q.; Wu, J.; Pan, Z.; Kong, X.; Cui, Z.; Wu, D.; Hu, G. Pt supported on boron, nitrogen co-doped carbon nanotubes (BNC NTs) for effective methanol electrooxidation. *Int. J. Hydrogen Energy* **2020**, *45*, 33634–33640. [CrossRef]